

Hydromechanical Response to Permeability Variations in a Simplified Dual-Well FEM Model Subjected to a Cycle of Injection and Extraction

Tomás Schmieder^a

(^a) School of Civil and Environmental Engineering, Cornell University
(tas274@cornell.edu)

Abstract: This study explores the hydro-mechanical behaviour of a simplified dual-well system in which one borehole injects and the other withdraws fluid in a controlled, cyclic pattern. The investigation focuses specifically on how different representations of permeability, both in magnitude and direction, govern the evolution of pore pressure and surface deformation in saturated porous media. A two-dimensional poro-elastic model was constructed using the MOOSE finite element framework. This model integrates Biot's theory of poroelasticity to capture the coupled interaction between fluid flow and mechanical response. Several permeability scenarios were evaluated, including isotropic cases with uniform conductivity in all directions, as well as anisotropic and cross-coupled tensor configurations that simulate directionally dependent flow behaviours. The results show that increasing permeability facilitates a transition from undrained to drained response conditions, with fluid pressure spreading more uniformly and surface deformation becoming more symmetric. In contrast, cases with low permeability displayed pressure fields that were more confined. Cases that were anisotropic lead to unique cases in both pressure and displacement patterns. The outcomes emphasize the importance of incorporating realistic tensor representations of permeability into models of subsurface behaviour. Demonstrating that both the size and orientation of permeability significantly shapes the geo-mechanical performance of fluid injection and withdrawal systems.

Keywords: borehole, cycle, displacement, finite element method, permeability, pressure, withdrawal

1 INTRODUCTION

1.1 Problem Introduction

Subsurface systems that rely on the injection and withdrawal of fluids, such as those used in geotechnical problems, geothermal energy extraction, and groundwater remediation, are strongly influenced by hydro-mechanical interactions between fluids and the porous solids (Wołoszyn et al., 2013). These interactions often lead to changes in pore pressure and mechanical deformation, which in turn affect system performance. Accurate predictions of these changes are essential in the design and operation of such engineering problems.

Permeability determines how easily fluid can flow through porous medium and affects the time scale over which pressure and deformation occurs. However, permeability is rarely a uniform property. Across geologic formations, permeability can vary in magnitude, isotopically, and often varies depending on direction. This anisotropy introduces additional complexity into the fluid-solid interaction, as directional differences in the medium can produce varying stress and pressure fields (Ding et al., 2019; Asaka et al., 2020). These complexities make it necessary to research tensor-based descriptions of permeability that account for both directional magnitude and potential off-diagonal coupling terms.

This project investigates how variations in permeability affect pore pressure and vertical displacement evolution in a simplified dual-well system. The setup includes one injection and one withdrawal borehole in a saturated porous domain. By varying permeability magnitude and tensor structure across

simulations, the study aims to clarify how these parameters influence hydromechanical behaviour under cyclic loading conditions.

1.2 Proposed Approach

The investigation begins with the construction of a two-dimensional plane-strain model that includes a borehole pair arranged symmetrically across the domain. One borehole acts as a fluid injection point while other a withdrawal point. The system is governed by Biot's theory of poroelasticity, which allows for the coupled treatment of fluid mass balance and mechanical deformation within a fully saturated porous material (Chen et al., 2016). The numerical model is implemented using the MOOSE finite element framework, which provides tools for simulating strongly coupled multi-physics systems, using the Porous Flow and Solid Mechanics modules.

Fluid is injected and withdrawn cyclically through the wells using a sinusoidal flux function. This loading pattern enables the study of how both pressure and deformation evolve over time. The model evaluates several permeability configurations, including isotropic conditions where flow behaves identically in all directions, as well as anisotropic tensors that assign higher permeability in one direction, as well as a cross-coupled tensor with off-diagonal terms that introduces more complex flow patterns.

Simulation results include spatial and temporal distributions of pore pressure and vertical displacement. These results are exported and analyzed using Python-based scripts to identify trends and differences across permeability cases. Attention is given to how the magnitude of permeability influences maximum and averages of both pressure and surface displacement, as well as how anisotropy modifies these outcomes. By only varying the permeability, this study will provide an understanding of how permeability creates responses in a simplified dual-well system under cyclic injection and withdrawal

1.3 Literature Review

Asaka et al. (2020) investigated the influence of permeability anisotropy on wellbore stability by developing a poro-elastic framework that allowed them to analyze stress and pore pressure distributions around a circular borehole. Their study demonstrated that directional differences in permeability alter the response of the surrounding formation, especially in terms of the predicted locations of failure. By solving the governing equations analytically, they showed that anisotropy introduces asymmetry in the stress field, even in geometrically simple domains. This finding emphasizes the importance of including directional flow characteristics when assessing borehole integrity. The conclusions drawn from their work lend direct support to the aims of the present study, where directional permeability is treated as a key variable in understanding surface uplift and pressure distribution.

Chen et al. (2016) developed an analytical model to study fluid injection into an isotropic poro-elastic medium. Their analysis focused on how time-dependent injection affects radial stress and pore pressure, using boundary conditions that mimic continuous injection scenarios. By coupling mechanical stress with pore pressure under anisotropic conditions, they revealed that permeability structure plays a large role in the evolution of stress distributions. Their findings are highly relevant to this study, which also investigates pressure-driven deformation under time-varying injection and withdrawal conditions.

Ding et al. (2019) extended the scope of poro-elastic wellbore modeling by incorporating the full permeability tensor into their formulation. They applied coordinate transformations on the tensor to explore more general anisotropic conditions, including cross-coupling effects. Their results found that anisotropy can change the critical pressure needed to cause boreholes to collapse, as well as modify the location of failure zones around the well. These outcomes are directly applicable to the present study, where a variety of tensor configurations are examined to determine how both magnitude and directionality affect pressure propagation and surface deformation. Their use of a complete tensorial representation justifies the inclusion of off-diagonal terms in our model.

Liakopoulos (1965) introduced the concept of a permeability tensor as a second-rank symmetric quantity capable of capturing directional flow behavior in anisotropic soils. He emphasized that, in materials such as these, the direction of hydraulic gradients may not be the same as the direction of fluid velocity, a consequence of anisotropic mediums. This distinction is important in understanding how off-axis flow components arise in cross-coupled systems.

Seib et al. (2022) used three-dimensional finite element modeling to study how spatial variations in hydraulic conductivity affect the performance of borehole-based thermal energy systems. Their analysis focused on fault zones with varying permeability structures and showed that even minor differences could substantially influence thermal efficiency. Although their primary concern was heat transfer rather than hydro-mechanical coupling, the methodology they employed offers insight for our study. In particular, their approach of varying materials within FEM simulations supports the decision to simulate a wide range of permeability values and orientations across different cases in this work.

Wilkins et al. (2021) presented a detailed overview of the MOOSE Porous Flow module, which serves as the numerical foundation for the current simulations. Their work outlines the capabilities of MOOSE in handling fully coupled problems that involve fluid flow, mechanical deformation, and chemical interactions in porous media. They described how varying permeabilities and other variables in MOOSE's input files allows for varying representation of isotropic and anisotropic materials. This directly relates to the present study, which uses MOOSE to simulate a range of tensor permeability cases under time-varying injection and withdrawal.

Wołoszyn et al. (2013) developed a finite element model for borehole heat exchangers that used one-dimensional elements to represent thin cylinders with radial variations. Their model, though focused on thermal conduction, addressed some of the same geometric challenges faced in the current study, such as steep pressure gradients near boreholes. By using reduced-dimensional elements and spatial variation in material properties, their work demonstrated that simplified geometries can still yield meaningful insights when combined with carefully designed simulations. These strategies support the modeling approach used in this study, in particular the choice of how the mesh is generated.

Yang et al. (2025) conducted a series of laboratory experiments to measure the permeability of various sandstone samples under different fluid types. Their work focused on how the type of fluid influences measured permeability, independent of other fluid-rock interactions. They found that the properties, such as pore geometry and connectivity, play a large role in determining permeability. This insight is important in the context of our study, which assumes a non-reactive fluid and holds material composition constant while only varying the permeability tensor. Yang's findings support the idea that structural differences by themselves can account for large variations in flow behavior, making it reasonable to isolate permeability as a primary variable in simulations of injection and withdrawal.

2 FEM PROBLEM FORMULATION

2.1 Governing Equations

The governing equations to model the problem of injection and withdrawal in 2D, with account for the deformability of the porous skeleton is the system of partial differential equations,

The governing equation for the solid phase:

$$-\alpha \nabla(p_w) + D_e : \nabla \epsilon = 0$$

The governing equation for the liquid phase:

$$\left(\frac{\alpha - \phi}{K_s} + \frac{\phi}{K_w} \right) \frac{D^s p_w}{Dt} + \alpha \frac{\partial \epsilon_v}{\partial t} = \frac{1}{\mu_k} \mathbf{k} : \nabla^2 p_w$$

These equations are derived from Biot's theory of poroelasticity.

2.2 Weak Formulation

We begin formulating the weak form for the finite element method through the use of the Ritz Method. We start by multiplying the governing equations by a test function such that integration by parts can be done. Let's begin with the governing equation for the solid phase,

$$-\alpha \nabla(p_w) + D_e : \nabla \epsilon = 0$$

Let v be a test function, we multiply our equation and integrate over its domain.

$$\forall v \sim \delta u, \quad \int_{\Omega} v \cdot (D_e : \nabla \epsilon) dV - \int_{\Omega} v \cdot \alpha \nabla p_w dV = 0$$

We can rewrite the first term using the symmetry of strain and stiffness tensors

$$\int_{\Omega} \nabla v : D_e : \epsilon dV - \int_{\Omega} \alpha \nabla p_w \cdot v dV = 0$$

$$\int_{\Omega} v \cdot \nabla \cdot \sigma' dV = - \int_{\Omega} \nabla v : \sigma' dV + \int_{\Gamma} v \cdot (\sigma' \cdot n) dS$$

We also assume natural boundary conditions, Neumann, therefore zero traction, allowing our boundary term to vanish, therefore our final weak form for the solid phase equation is,

$$\int_{\Omega} \nabla v : D_e : \epsilon(u) dV = \int_{\Omega} \alpha \nabla p_w \cdot v dV$$

We can now begin the weak formulation for the governing equation of the liquid phase,

$$\left(\frac{\alpha - \phi}{K_s} + \frac{\phi}{K_w} \right) \frac{D^s p_w}{Dt} + \alpha \frac{\partial \epsilon_v}{\partial t} = \frac{1}{\mu_k} k : \nabla^2 p_w$$

We can start by simplifying notation,

$$C = \left(\frac{\alpha - \phi}{K_s} + \frac{\phi}{K_w} \right), \quad q = -\frac{k}{\mu} \nabla p_w$$

$$C \frac{D^s p_w}{Dt} + \alpha \frac{\partial \epsilon_v}{\partial t} = \nabla q$$

Multiply the equation by a test function w and integrate over the domain,

$$\forall w \sim \delta p_w, \quad \int_{\Omega} w \left(C \frac{\partial p_w}{\partial t} + \alpha \frac{\partial \epsilon_v}{\partial t} \right) dV = - \int_{\Omega} w \nabla \cdot q dV$$

Using the divergence theorem,

$$- \int_{\Omega} w \nabla \cdot q dV = \int_{\Omega} \nabla w \cdot q dV - \int_{\Gamma} w (q \cdot n) dS$$

Assuming Neumann, zero-flux boundaries, the boundary term vanishes, therefore the final weak form for the liquid phase can be written as,

$$\int_{\Omega} w \left(C \frac{\partial p_w}{\partial t} + \alpha \frac{\partial \epsilon_V}{\partial t} \right) dV + \int_{\Omega} \nabla w \cdot \left(\frac{\mathbf{k}}{\mu} \nabla p_w \right) dV = 0$$

2.3 Space Discretization

We must now begin space discretization so that we can convert the weak form into a discrete system of algebraic equations through approximating the fields using finite-dimensional function spaces, using shape function on mesh elements. We begin by noting our FEM test function approximations as shape functions,

$$\mathbf{u} \approx \sum_j \mathbf{N}_j \hat{\mathbf{u}}_j, \quad \mathbf{v} \approx \sum_i \mathbf{N}_i \delta \mathbf{u}_i, \quad p_w \approx \sum_j N_j \hat{p}_j, \quad w \approx \sum_i N_i \delta p_i$$

Where N_i, \mathbf{N}_i are shape functions, scalar for pressure, and vector for displacement, and $\hat{\mathbf{u}}_j, \hat{p}_j$ are nodal values. After discretization the solid phase equation can be written as,

$$\sum_{i,j} \delta \mathbf{u}_i^T \left[\int_{\Omega} \nabla \mathbf{N}_i : \mathbf{D}_e : \nabla \mathbf{N}_j dV \right] \hat{\mathbf{u}}_j = \sum_i \delta \mathbf{u}_i^T \left[\int_{\Omega} \alpha \nabla p_w \cdot \mathbf{N}_i dV \right]$$

Similarly, the discretized form of the liquid phase equation can be written as,

$$\sum_{i,j} \delta p_i \left[\int_{\Omega} C N_i N_j dV \right] \frac{d\hat{p}_j}{dt} + \sum_{i,j} \delta p_i \left[\int_{\Omega} \nabla N_i \cdot \frac{\mathbf{k}}{\mu} \nabla N_j dV \right] \hat{p}_j + \sum_i \delta p_i \left[\int_{\Omega} \alpha N_i \frac{d}{dt} (\nabla \cdot \mathbf{u}) dV \right] = 0$$

The discretized solid phase equation leads to the global stiffness matrix \mathbf{K}_{uu} and coupling matrix \mathbf{K}_{up} , the discretized liquid phase equation leads to the mass matrix \mathbf{M}_{pp} , the diffusion matrix \mathbf{K}_{pp} and the second coupling term \mathbf{K}_{pu} . This ultimately leads to the discretized system of the form,

$$\begin{bmatrix} \mathbf{K}_{uu} & \mathbf{K}_{up} \\ \mathbf{K}_{pu} & \mathbf{M}_{pp} + \mathbf{K}_{pp} \end{bmatrix} \begin{bmatrix} \mathbf{u} \\ p \end{bmatrix} = \begin{bmatrix} \mathbf{f}_u \\ \mathbf{f}_p \end{bmatrix}$$

Where \mathbf{u} and p are the unknown displacements and pressures.

2.4 Time Discretization

The system solves the transient evolution of the model using the backward Euler method, in conjunction with a Newton-Raphson nonlinear solver. The backwards Euler method takes the form of,

$$\frac{p^{n+1} - p^n}{\Delta t}, \frac{\mathbf{u}^{n+1} - \mathbf{u}^n}{\Delta t}$$

The discrete form of the fluid mass balance equation can be written as,

$$\mathbf{M}_{pp} \frac{p^{n+1} - p^n}{\Delta t} + \mathbf{K}_{pu} \frac{\mathbf{u}^{n+1} - \mathbf{u}^n}{\Delta t} + \mathbf{K}_{pp} p^{n+1} = \mathbf{f}_p^{n+1}$$

$$\left(\frac{1}{\Delta t} \mathbf{M}_{pp} + \mathbf{K}_{pp} \right) p^{n+1} + \frac{1}{\Delta t} \mathbf{K}_{pu} \mathbf{u}^{n+1} = \frac{1}{\Delta t} \mathbf{M}_{pp} p^n + \frac{1}{\Delta t} \mathbf{K}_{pu} \mathbf{u}^n + \mathbf{f}_p^{n+1}$$

The solid momentum equation can be written as,

$$\mathbf{K}_{uu} \mathbf{u}^{n+1} + \mathbf{K}_{up} p^{n+1} = \mathbf{f}_u^{n+1}$$

In block matrix form the final time marching system is,

$$\begin{bmatrix} \mathbf{K}_{uu} & \mathbf{K}_{up} \\ \frac{1}{\Delta t} \mathbf{K}_{pu} & \frac{1}{\Delta t} \mathbf{M}_{pp} + \mathbf{K}_{pp} \end{bmatrix} \begin{bmatrix} \mathbf{u}^{n+1} \\ p^{n+1} \end{bmatrix} = \begin{bmatrix} \mathbf{f}_u^{n+1} \\ \mathbf{r}_p \end{bmatrix}$$

Where the right-hand side of the fluid system includes known values of,

$$\mathbf{r}_p = \frac{1}{\Delta t} \mathbf{M}_{pp} p^n + \frac{1}{\Delta t} \mathbf{K}_{pu} \mathbf{u}^n + \mathbf{f}_p^{n+1}$$

2.5 Mesh Description

The computational domain is a 2D rectangular region measuring 50 meters in width and 25 meters in height. Two circular wells are embedded within the domain as holes: an injection well centered at (15, 12.5) and a withdrawal well centered at (35, 12.5), each with a radius of 1 meter. Each circular hole represents a slice of a borehole. The mesh is generated in Gmsh using distance-based refinement, specifically: within 1 meter of either well, the mesh element size is refined to 0.5 meters, beyond 5 meters from either well, the element size coarsens to 2.0 meters, between 1 and 5 meters the element size is determined by linear interpolation between the two limits. This grading strategy provides fine resolution near the wells, where pressure and displacement gradients are steepest due to injection and withdrawal fluxes. Coarser elements are used in the outer region of the domain to reduce computational cost without sacrificing accuracy near critical features (Wołoszyn et al., 2013).

3 MODEL METHODOLOGY

3.1 Simulation Introduction

The finite element method system is simulated through the use of MOOSE, an open-source parallel finite element framework. MOOSE is used to solve the fully coupled hydro-mechanical equations that govern fluid flow and deformation in a porous medium surrounding a dual-well borehole system. The simulations are carried out using the Porous Flow and Solid Mechanics, modules, specifically designed to model multiphase flow and mechanical deformation in saturated and unsaturated porous materials (Wilkins et al. 2022). Simulations were run on a 2D rectangular domain containing the two circular wells. Data was taken over a line going through the middle of the domain, the data was solved using a backward Euler time-stepping scheme and Newton-Raphson iterations. Output data included pore pressure and vertical surface displacement vs. time and radius, which were post-processed and analyzed using Python.

3.2 Material Properties & Boundary Conditions

The model solves the fully coupled hydro-mechanical Biot system, consisting of the solid momentum balance and fluid mass conservation equations. The solid is modelled as a linearly elastic material with a Young's modulus of 5×10^{-9} Pa and a Poisson's ration of 0.3, appropriate for small strain geomechanical deformation. The medium has a constant porosity of 0.2, while the permeability tensor is varied across simulation cases to explore material-dependent flow behaviour.

The fluid phase is initialized with a hydrostatic pore pressure of 1 MPa, and the initial displacement field is set to zero. Boundary conditions are applied as follows:

- The left and right edges of the domain are assigned Dirichlet pressure conditions of 1 MPa
- The well boundaries receive a time-dependent sinusoidal flux:

$$q(t) = \pm 10000 \cdot \frac{315 \times 10^{-6}}{2\pi \cdot 1 \cdot 20} \cdot \sin\left(\frac{2\pi t}{500}\right)$$

This expression corresponds to an approximate flow rate of 5 gallons/minute a representative measurement of injection or withdrawal, the magnitude increase allows for a better visual and numerical result to understand the changes in pressure and surface displacement, modelled sinusoidally over a 500-second period. The injection well receives a positive flux, while the abstraction well receives the corresponding negative flux.

- The left and right boundaries are fixed in the horizontal direction to prevent lateral movement.
- The bottom boundary is fixed vertically to simulate a mechanically supported base.
- The top surface is traction-free, allowing vertical displacement in response to evolving pressure gradients.
- All interior nodes are free to respond dynamically to pore pressure induced stress changes, enabling realistic hydromechanical coupling

These conditions together provide a well-posed system for simulating surface uplift, pressure diffusion, and mechanical deformation due to borehole injection and withdrawal in a plane strain domain.

3.3 Permeability Tensor

This study investigates how variations in permeability influence pore pressure evolution and surface displacement in a coupled hydro-mechanical system. Permeability in porous media is described by a second-order tensor \mathbf{k} , which, in three dimensions, is a symmetric 3×3 matrix:

$$\mathbf{k} = \begin{bmatrix} k_{xx} & k_{xy} & k_{xz} \\ k_{yx} & k_{yy} & k_{yz} \\ k_{zx} & k_{zy} & k_{zz} \end{bmatrix}$$

However, because this model is two-dimensional and restricted to the XY plane, only the upper-left 2×2 , submatrix is active,

$$\mathbf{k}_{2D} = \begin{bmatrix} k_{xx} & k_{xy} \\ k_{yx} & k_{yy} \end{bmatrix}$$

Each component of the tensor has a physical interpretation:

- k_{xx} : Permeability in the x-direction due to a pressure gradient in x
- k_{yy} : Permeability in the y-direction due to a pressure gradient in y
- k_{xy} : Flow in the x-direction induced by a pressure gradient in y
- k_{yx} : Flow in the y-direction induced by a pressure gradient in x

In isotropic media, the off-diagonal terms vanish. However, in anisotropic or cross-coupled materials, these terms may differ, allowing for directionally dependent and rotated flow behaviour.

3.4 Permeability Tests

The model tests different permeability tensor values as defined above, such tests are representative of isotropic materials, which are defined below,

Permeability Value (m^2)	Permeability Tensor	Description
10^{-20}	$\begin{bmatrix} 10^{-20} & 0 \\ 0 & 10^{-20} \end{bmatrix}$	Near-impermeable; fluid flow is almost completely obstructed; approximates an undrained condition
10^{-16}	$\begin{bmatrix} 10^{-16} & 0 \\ 0 & 10^{-16} \end{bmatrix}$	Very low permeability: fluid migration is severely limited

10^{-13}	$\begin{bmatrix} 10^{-13} & 0 \\ 0 & 10^{-13} \end{bmatrix}$	Moderately low permeability; permits slow fluid movement
10^{-10}	$\begin{bmatrix} 10^{-10} & 0 \\ 0 & 10^{-10} \end{bmatrix}$	Allows efficient fluid flow across domain
10^{-07}	$\begin{bmatrix} 10^{-07} & 0 \\ 0 & 10^{-07} \end{bmatrix}$	High permeability, offering minimal resistance to flow

Table 1. Isotropic Permeability & Material Values used in Simulation

The model also tests permeability tensor configurations that are anisotropic and cross-coupled,

Test	Permeability Tensor	Description
X High	$\begin{bmatrix} 10^{-10} & 0 \\ 0 & 10^{-15} \end{bmatrix}$	High permeability in x-direction, low in y-direction; strong directional flow along x
Y High	$\begin{bmatrix} 10^{-15} & 0 \\ 0 & 10^{-10} \end{bmatrix}$	High permeability in y-direction, low in x-direction; strong directional flow along y
Y Blocked	$\begin{bmatrix} 10^{-15} & 0 \\ 0 & 10^{-20} \end{bmatrix}$	Very low permeability in both directions, especially nearly impermeable in y
Cross-Coupled	$\begin{bmatrix} 10^{-13} & 10^{-13} \\ 10^{-13} & 10^{-13} \end{bmatrix}$	Strongly anisotropic and cross-coupled medium; all components equal, allowing non-directional flow and coupling between directions.

Table 2. Anisotropic Permeability Values used in Simulation

Isotropic materials serve as a baseline to evaluate the role of permeability magnitude in pressure transmission and deformation, where directional effects are absent. In contrast, the anisotropic and cross-coupled cases simulate more realistic media where materials are varying and not constant. By testing both isotropic and anisotropic permeability tensors, this study better evaluates how the permeability of materials in dual-well hydro-mechanical systems can influence changes in pore pressure and surface displacement.

4 SIMULATION RESULTS

4.1 Isotropic Permeability Simulation Results

The results of simulations graphing the change in pore pressure and surface displacement vs. radius and time for the isotropic test cases can be found below,

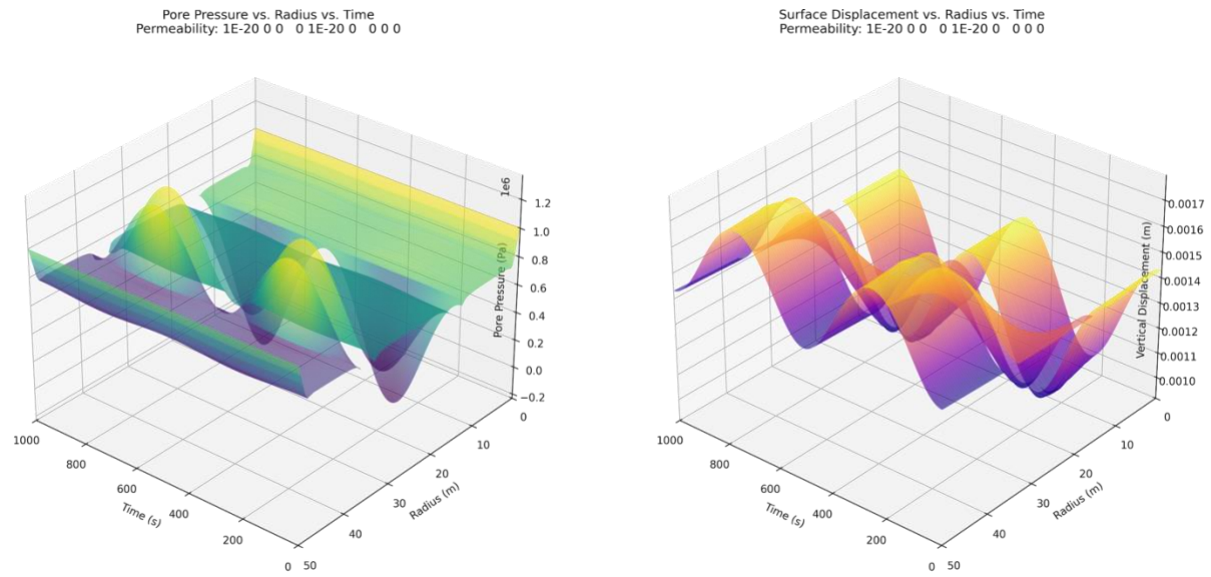


Figure 1. Pressure and Surface Displacement vs. Time and Radius for Permeability of 1×10^{-20}

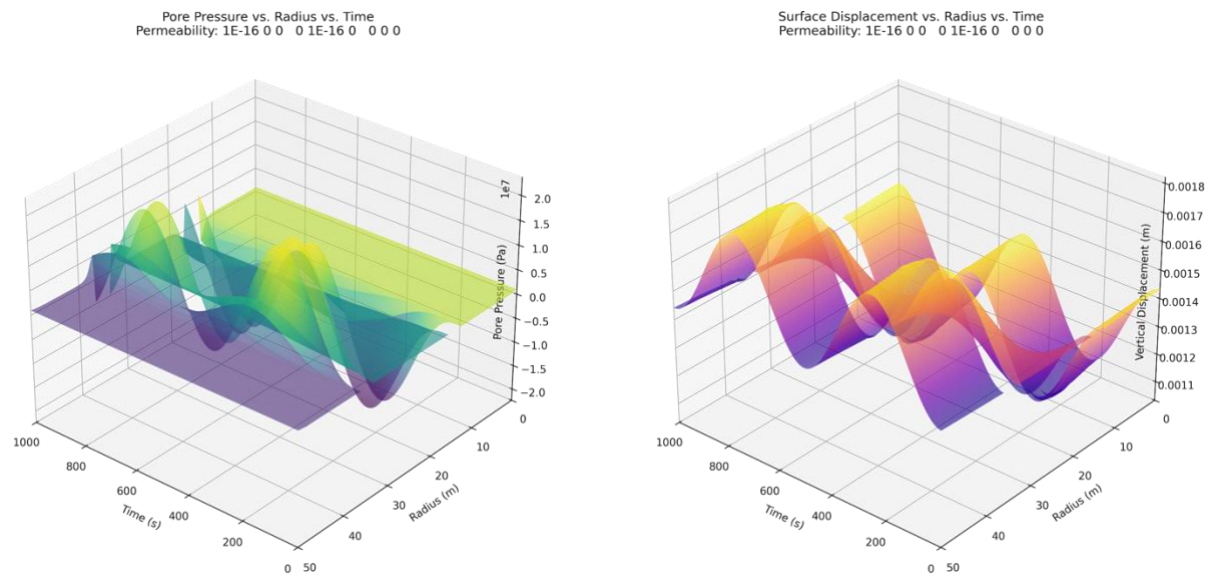


Figure 2. Pressure and Surface Displacement vs. Time and Radius for Permeability of 1×10^{-16}

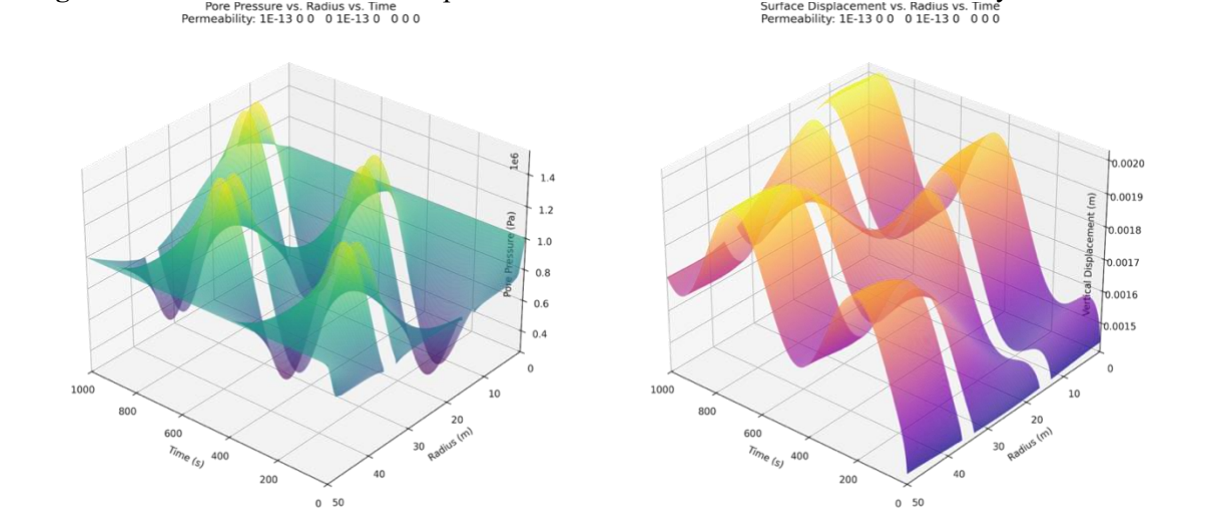


Figure 3. Pressure and Surface Displacement vs. Time and Radius for Permeability of 1×10^{-13}

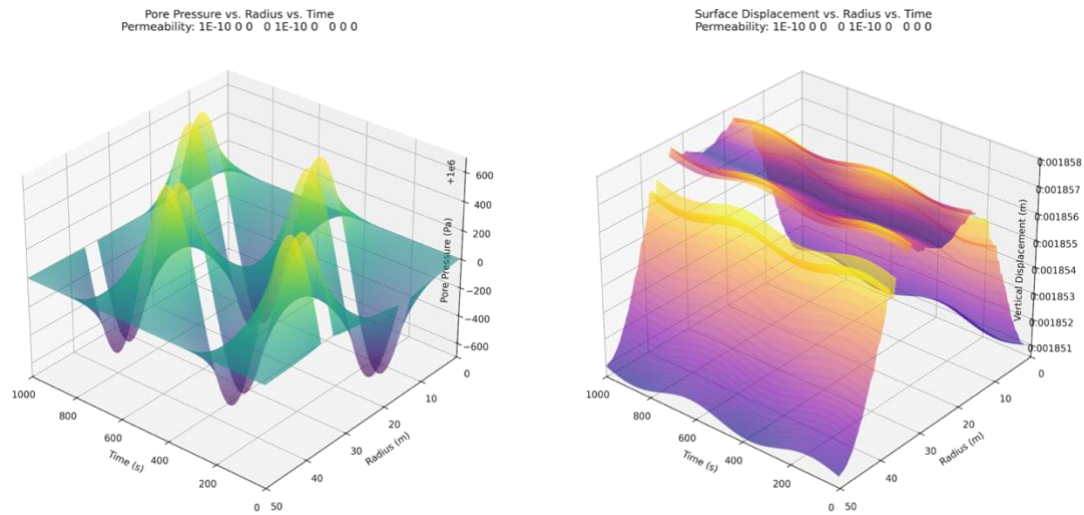


Figure 4. Pressure and Surface Displacement vs. Time and Radius for Permeability of 1×10^{-10}

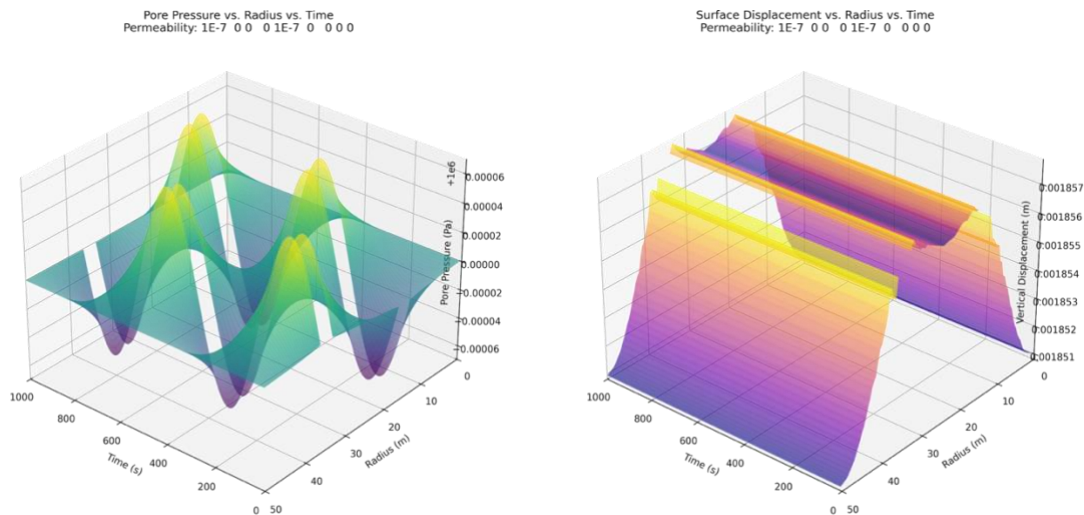


Figure 5. Pressure and Surface Displacement vs. Time and Radius for Permeability of 1×10^{-07}

The numerical simulation outputs were post-processed to extract values of pore pressure and vertical surface displacement, maximums and averages of these values were computed and can be found below,

Permeability Value (m^2)	Maximum Pressure (MPa)	Average Pressure (MPa)
10^{-20}	1.3356323	0.7634145
10^{-16}	22.6956323	0.7672013
10^{-13}	1.520637	0.9454388
10^{-10}	1.0006704	0.999943
10^{-07}	1	1

Table 3. Isotropic Permeability Pressure Results

Permeability Value (m^2)	Maximum Surface Displacement (m)	Average Surface Displacement (m)
10^{-20}	0.0017778	0.00114595
10^{-16}	0.0018047	0.0014834
10^{-13}	0.0020158	0.0017853
10^{-10}	0.0018579	0.0018571
10^{-07}	0.0018577	0.0018572

Table 4. Isotropic Permeability Surface Displacement Results

4.2 Isotropic Permeability Results Discussion

The isotropic permeability reveals a trend in how the magnitude of permeability affects both pressure distribution and surface displacement. At lower tested permeability values, the fluid flow is significantly restricted, this resulted in lower amounts of average pressure as well as average surface displacement. As permeability increases, pressure builds more rapidly, creating large maximums for $10^{-13} m^2$ near the injection zone, but full propagation across the domain remains impeded, creating steeper pressure gradients and slightly greater displacement. Once permeability reaches $10^{-10} m^2$ and higher, pressure equilibrates quickly across the domain. The pore pressure and surface displacement reach nearly uniform values. At $10^{-07} m^2$, the domain effectively acts as a fluid reservoir with minimal resistance, with pressure and deformation reaching their maximum theoretical values under cyclic loading. These results emphasize the transition from undrained to drained response with increasing permeability. Despite their being a trend between these three permeability values, once values become greater than $10^{-13} m^2$, the trend for maximum pressure values seems to go off course with $10^{-16} m^2$ having an abnormally high maximum pressure followed by the $10^{-20} m^2$ value being relatively small. This abnormality may be a result of transitional drainage behaviour, where the permeability is low enough to restrict outflow but high enough to permit rapid local buildup of fluid near the injection well. The system may behave undrained early in the cycle, resulting in temporary pressure spikes before full dissipation occurs. Additionally, the numerical resolution or time-stepping choices may contribute to this estimations of local peak pressures.

4.3 Anisotropic Permeability Simulation Results

The results of simulations graphing the change in pore pressure and surface displacement vs. radius and time for the anisotropic test cases can be found below,

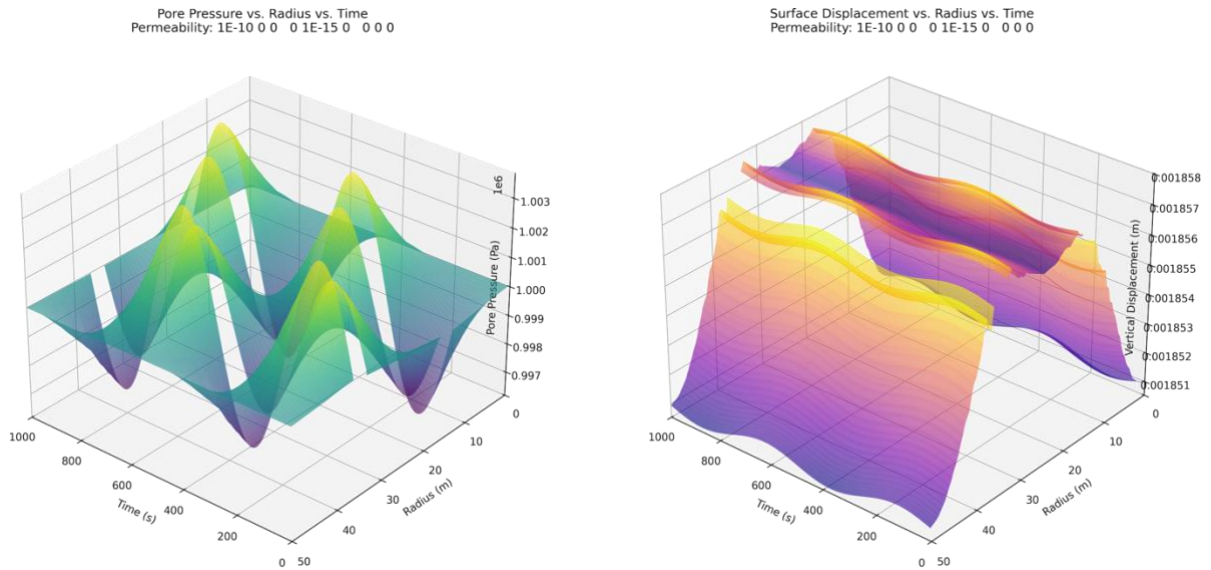


Figure 6. Pressure and Surface Displacement vs. Time and Radius for Anisotropic Case: X High

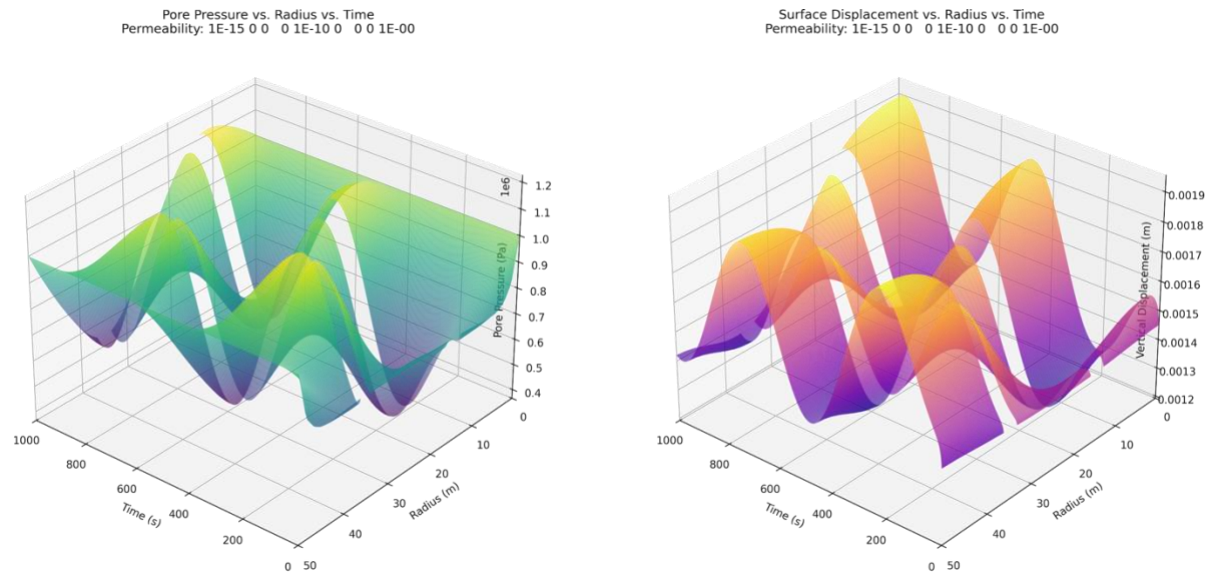


Figure 7. Pressure and Surface Displacement vs. Time and Radius for Anisotropic Case: Y High

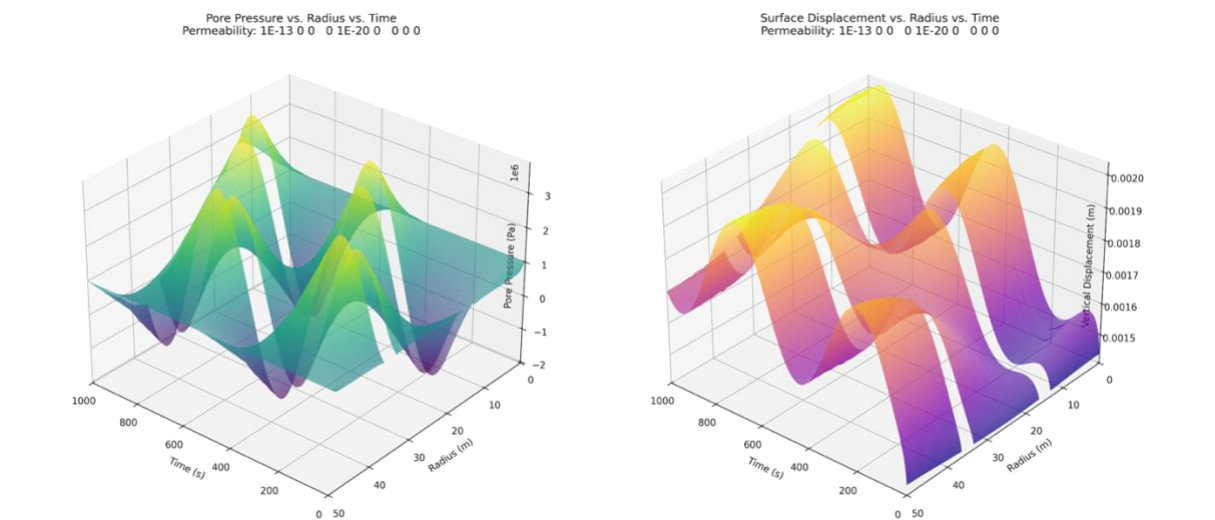


Figure 8. Pressure and Surface Displacement vs. Time and Radius for Anisotropic Case: Y Blocked

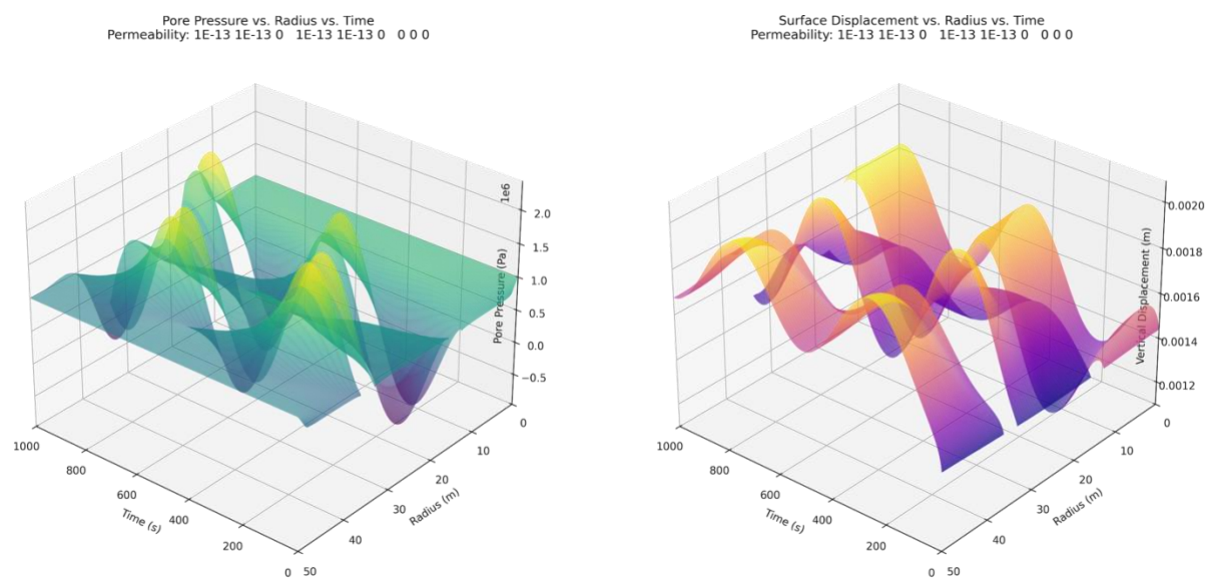


Figure 9. Pressure and Surface Displacement vs. Time and Radius for Anisotropic Case: Cross Coupled

The numerical simulation outputs were post-processed to extract values of pore pressure and vertical surface displacement, maximums and averages of these values were computed and can be found below,

Case	Permeability Tensor	Maximum Pressure (MPa)	Average Pressure (MPa)
X High	$\begin{bmatrix} 10^{-10} & 0 \\ 0 & 10^{-15} \end{bmatrix}$	1.0036735	0.9999231
Y High	$\begin{bmatrix} 10^{-15} & 0 \\ 0 & 10^{-10} \end{bmatrix}$	1.2082272	0.8509174
Y Blocked	$\begin{bmatrix} 10^{-15} & 0 \\ 0 & 10^{-20} \end{bmatrix}$	3.7452244	0.9296603
Cross-Coupled	$\begin{bmatrix} 10^{-13} & 10^{-13} \\ 10^{-13} & 10^{-13} \end{bmatrix}$	2.3559127	0.8985141

Table 5. Anisotropic Permeability Pressure Results

Case	Permeability Tensor	Maximum Surface Displacement (m)	Average Surface Displacement (m)
X High	$\begin{bmatrix} 10^{-10} & 0 \\ 0 & 10^{-15} \end{bmatrix}$	0.0018579	0.0018571
Y High	$\begin{bmatrix} 10^{-15} & 0 \\ 0 & 10^{-10} \end{bmatrix}$	0.0019394	0.0016309
Y Blocked	$\begin{bmatrix} 10^{-15} & 0 \\ 0 & 10^{-20} \end{bmatrix}$	0.0020252	0.0017824
Cross-Coupled	$\begin{bmatrix} 10^{-13} & 10^{-13} \\ 10^{-13} & 10^{-13} \end{bmatrix}$	0.0020701	0.00174

Table 6. Anisotropic Permeability Surface Displacement Results

4.4 Anisotropic Permeability Results Discussion

Anisotropic permeability cases exhibit more complex behaviour due to directional differences in fluid conductivity. In the X High case, high horizontal permeability allows fluid to spread efficiently along the x-axis between wells, while vertical movement is constrained. This results in fast pressure equalization across the midplane and a highly symmetric displacement profile. Conversely, in the Y High case, vertical permeability dominates, but horizontal flow between the wells is restricted. This causes pressure to build up near the injection well, leading to a higher maximum pressure but overall, less average pressure. The Y Blocked case shows extreme vertical confinement, effectively decoupling the wells hydrologically. The result is a sharp pressure spike near the injection zone, with most of the surface uplift concentrated immediately above the injection well. The cross-coupled case, where all tensor components are equal, exhibits behaviour between the high and low permeability extremes. The coupling terms induce flow across both axes even in the absence of aligned gradients, enabling a broader spread of pressure and surface displacement. Though initially considered isotropic in magnitude, the cross terms act to “rotate” the effective permeability tensor, redistributing flow paths (Liakopoulos, 1965). This led to higher overall maximum pressure values, but little to no change in the both the averages for pore pressure and surface displacement

4.5 Results Discussion

Figures below for a contour of each test case were taken out at a time of $t = 500$ s for pressure vs. radius, as well as surface displacement vs. radius,

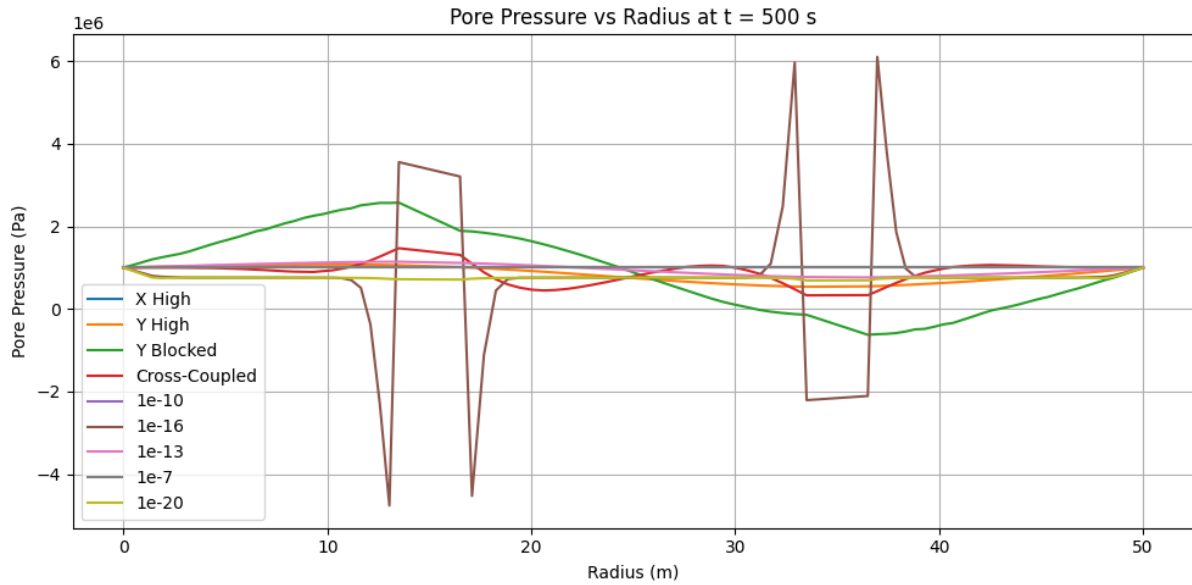


Figure 10. Pressure vs. Radius at $t = 500$ s for all Cases

For high permeability cases, pressure equilibrates efficiently between the injection and withdrawal wells, producing nearly flat profiles indicating minimal hydraulic resistance. In contrast, the low-permeability cases exhibit sharp pressure gradients localized near the wells, reflecting their undrained behaviour. The case of $10^{-16}m^2$ continues to show abnormal behaviours when graphing their contour for pressure, with incredibly steep pressure gradients by the wells. To better visualize the remaining cases the $10^{-16}m^2$ curve was excluded from the following curve,

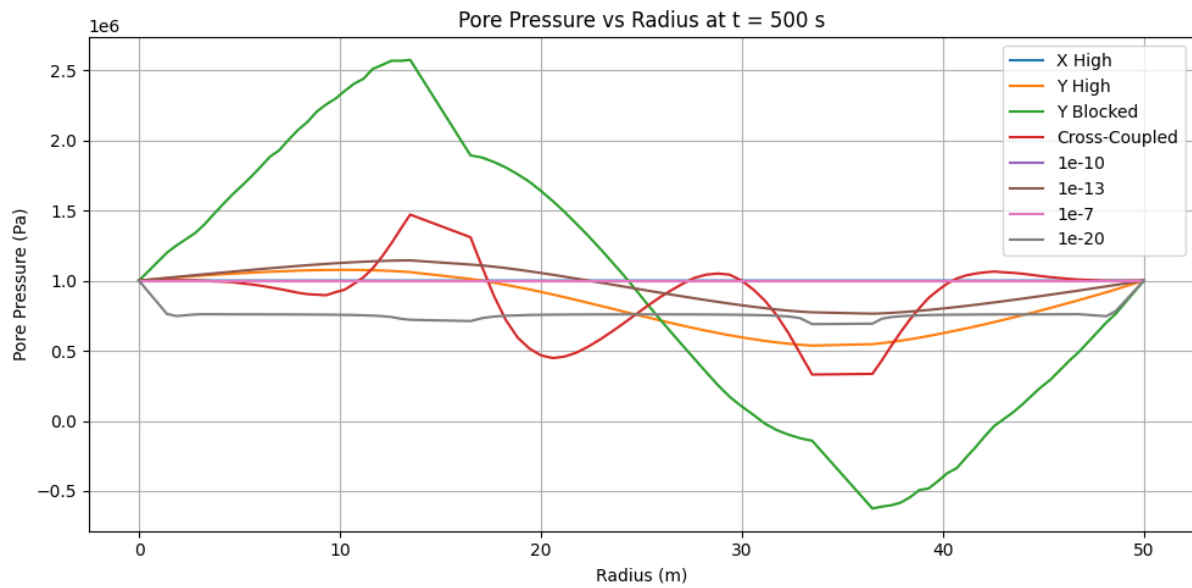


Figure 11. Pressure vs. Radius at $t = 500$ s ($10^{-16}m^2$ case removed)

The removal of the $10^{-16}m^2$ case allows for better viewing of the patterns exhibited between permeability and changes in pressure. The cleaned plot reveals the expected trend of increasingly sharp gradients with decreasing isotropic permeability and illustrates the stabilizing role of higher permeabilities in dissipating pressure over time and space.

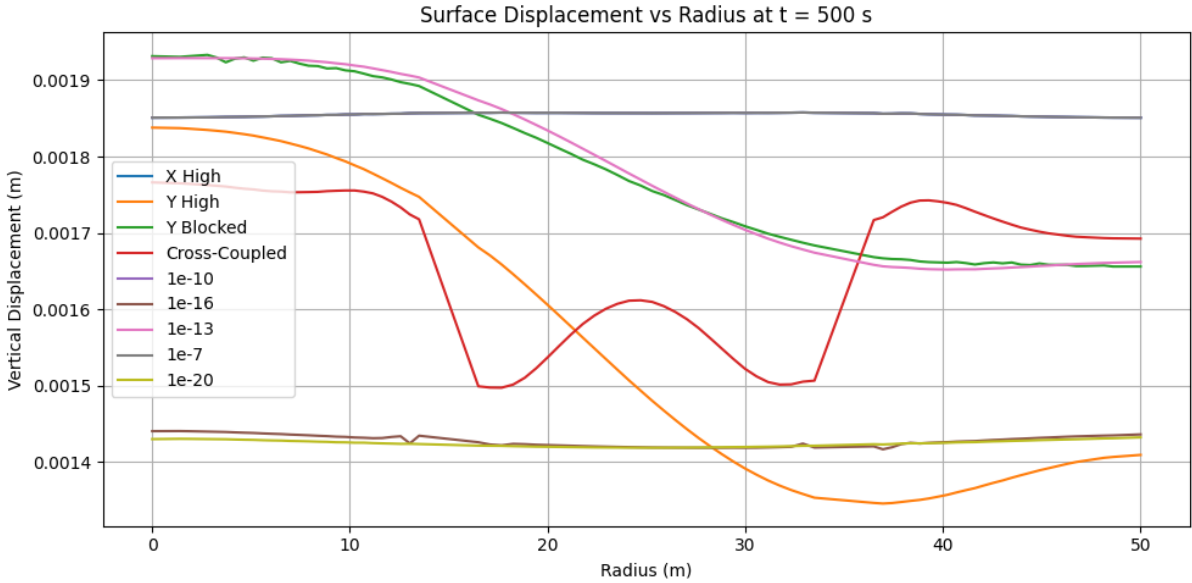


Figure 12. Surface Displacement vs. Radius at $t = 500$ s for all Cases

High permeability cases, as well as the X High anisotropic case result in broad and uniform displacement profiles, with uplift distributed symmetrically around the domain center. This aligns with their ability to transmit fluid pressure informally, inducing more consistent mechanical deformation. The Y High case exhibits a similar pattern but of larger magnitude. Much smaller isotropic permeability cases show much less surface displacement than the others. The cross-coupled case displays a more irregular, oscillatory displacement pattern, suggesting that the off-diagonal tensor terms induce more complex directional stress redistribution. Together, these plots confirm that permeability not only controls fluid transport but also causes changes in spatial patterns of mechanical response, emphasizing the value of tensor permeability modelling for subsurface simulations.

4.6 Discrepancies

While the numerical results generally align with physical expectations and analytical trends, discrepancies were observed. Most notably, the isotropic case of $10^{-16} m^2$ produced abnormally sharp spikes in pore pressure near both the injection and withdrawal wells, deviating from otherwise smooth progression seen across the permeability spectrum, resulting in an abnormally large maximum pressure. This irregularity may result from the material being a transition state between drained and undrained conditions, where pore pressure builds up rapidly but lacks sufficient permeability to diffuse efficiently during the injection and withdrawal cycle. Additionally, numerical artifacts related to time integration or spatial discretization could amplify local pressure gradients, particularly near the flux boundary where steep gradients form, and small mesh cells may dominate. A coarse or uneven mesh, coupled with a fixed timestep size in the backward Euler scheme, may lead to local overshoot or under-resolved gradients in this intermediate permeability regime.

Another discrepancy is a slight asymmetry in the cross-coupled permeability case, which theoretically should exhibit symmetric behaviour given the equality of all tensor components. The observed asymmetry may arise from interactions between the cross terms and boundary geometry, especially in a discretized domain where small inconsistencies in node alignment or integration point orientation on the mesh can lead to differences. Furthermore, small surface displacement artifacts that appear as noise are noted near the domain boundaries in the Y Blocked case. These are likely the result of the boundary condition interactions with the mesh refinement, where there is more noise near the boundary, and it smooths out closer to the location of the wells where the mesh is more refined. These minor fluctuations do not affect the core analysis but highlight the importance of meshing and the limitations of using a coarse mesh.

Overall, while these discrepancies are localized and do not necessarily undermine the core trends of the study, they underscore the need for a possible sensitivity analysis, with finer meshing, and possible timestep adaptation when exploring permeability at critical values.

5 CONCLUSIONS

5.1 Conclusion

This study examined how permeability affects fluid pressure and surface movement in a dual-well system. The wells operate using repeated injection and withdrawal cycles. We modelled the system using Biot's poro-elastic theory and implemented it in the MOOSE finite element framework. Simulations tested a wide range of permeability types, including isotropic, anisotropic, and cross-coupled tensors.

Low-permeability cases produced sharp pressure gradients and limited fluid movement. These cases also showed more localized surface uplift. In contrast, high-permeability domains allowed pressure to spread more evenly, resulting in smoother and more symmetric deformation. Simulations with directional permeability produced asymmetric pressure fields and uneven uplift patterns.

One intermediate case, with a permeability of $10^{-16}m^2$, behaved in an unexpected way. This suggests that some permeability effects may not follow a simple trend. More detailed study may be needed for mid-range cases.

Overall, the results show that both the size and the direction of permeability matter. Full tensor models provide more realistic predictions. Cyclic loading is also a useful tool for studying how systems respond to changing pressure.

5.2 Limitations

Although the model presented in this study provides valuable insights, several limitations must be acknowledged. First, the material behavior was assumed to be linearly elastic with constant porosity. These assumptions simplify the analysis but may not reflect the true behavior of real geologic materials, which often evolve under mechanical and chemical influences. In practice, porosity and stiffness may change in response to stress, fluid saturation, or other dynamic factors.

The model also assumes that permeability remains constant over time. This excludes the possibility of permeability evolution due to fracturing, compaction, or chemical interactions, all of which are known to affect fluid flow in natural systems. Including such effects would require a more complex constitutive framework and additional parameters that were beyond the scope of the current analysis.

The two-dimensional plane strain assumption further limits the generalizability of the findings. While this simplification reduces computational costs, it neglects three-dimensional effects such as out-of-plane stresses and flow components. Real borehole systems operate in fully three-dimensional environments, and future work should aim to incorporate three-dimensional geometry to capture these additional effects.

The boundary conditions and input fluxes were also idealized. The sinusoidal flux function provides a convenient test case for cyclic behaviour, but actual well operations often involve irregular flow rates, operational constraints, and feedback mechanisms. These real-world factors introduce variability that is not captured in the current setup.

From a numerical perspective, the model used fixed time stepping and a uniform mesh resolution. These settings may not fully capture steep gradients or evolving pressure fronts, particularly in the abnormal transitional permeability case. The unexpected results observed in the intermediate permeability

scenario suggest that a finer mesh or adaptive time stepping could improve accuracy and stability. These refinements would allow for better resolution of localized effects and might help explain the nonlinear behaviour observed in some cases.

Despite these limitations, the study provides a solid baseline for exploring hydro-mechanical coupling in porous media. The framework can be extended to incorporate evolving material properties, more realistic geometries, and complex boundary conditions. These improvements would make the model more applicable to real engineering systems, especially in fields like geothermal energy, carbon sequestration, and subsurface waste disposal.

NOTATIONS

α	biot coefficient
D_e	elastic stiffness tensor
p_w	pore fluid pressure
ϵ	strain tensor
ϕ	porosity
K_s	bulk modulus of the solid
K_w	bulk modulus of the fluid
ϵ_V	volumetric strain
μ_k	dynamic viscosity of the pore fluid
\mathbf{k}	permeability tensor
σ'	effective stress tensor
∇	gradient operator
q	darcy flux
K_{uu}	stiffness matrix for displacement
K_{up}	coupling matrix from pressure to displacement
M_{pp}	mass matrix for pressure
K_{pp}	diffusion matrix for pressure field
K_{pu}	coupling matrix from displacement to pressure
\mathbf{u}	displacement vector
$\delta \mathbf{u}, \mathbf{v}$	test function for displacement
$\delta p_w, \mathbf{w}$	test function for pore pressure
N_i, N_j	shape functions to interpolate scalar fields
$\mathbf{N}_i, \mathbf{N}_j$	shape functions to interpolate vector fields
\hat{u}_j, \hat{p}_j	nodal values of displacement and pressure
Δt	time step
$\frac{D^s p_w}{Dt}$	derivative of pore pressure

REFERENCES

- Asaka, M., & Holt, R. M. (2020). Anisotropic Wellbore Stability Analysis: Impact on Failure Prediction. *Rock Mechanics and Rock Engineering*.
<https://doi.org/10.1007/s00603-020-02283-0>
- Chen, S. L., & Abousleiman, Y. N. (2016). Stress analysis of borehole subjected to fluid injection in transversely isotropic poroelastic medium. *Mechanics Research Communications*, 73, 63–75.
<https://doi.org/10.1016/j.mechrescom.2016.02.003>
- Ding, L., Wang, Z., Liu, B., Jianguo Lv, & Wang, Y. (2019). Borehole stability analysis: A new model considering the effects of anisotropic permeability in bedding formation based on poroelastic theory. *Journal of Natural Gas Science and Engineering*, 69, 102932–102932.
<https://doi.org/10.1016/j.jngse.2019.102932>
- Liakopoulos, A. C. (1965). Variation of the permeability tensor ellipsoid in homogeneous anisotropic soils. *Water Resources Research*, 1(1), 135–141. <https://doi.org/10.1029/wr001i001p00135>
- Seib, L., Welsch, B., Bossennec, C., Frey, M., & Sass, I. (2022). Finite element simulation of permeable fault influence on a medium deep borehole thermal energy storage system. *Geothermal Energy*, 10(1). <https://doi.org/10.1186/s40517-022-00224-4>
- Wilkins, A., Green, C. P., & Ennis-King, J. (2021). An open-source multiphysics simulation code for coupled problems in porous media. *Computers & Geosciences*, 154, 104820.
<https://doi.org/10.1016/j.cageo.2021.104820>
- Wołoszyn, J., & Gołaś, A. (2013). Modelling of a borehole heat exchanger using a finite element with multiple degrees of freedom. *Geothermics*, 47, 13–26.
<https://doi.org/10.1016/j.geothermics.2013.01.002>
- Yang, X., Kang, B., Xu, B., Wang, H., Zhou, C., Jiang, K., & Li, X. (2025). Experimental study of rock permeability in different fluid media: a case study of two clay-free sandstones. *Frontiers in Earth Science*, 12. <https://doi.org/10.3389/feart.2024.1512685>